Microwave Capillary Discharges in Helium at Atmospheric Pressure

Miguel Ângelo Correia dos Santos
Instituto de Plasmas e Fusão Nuclear
Instituto Superior Técnico
July 2013

Abstract

This work uses both simulations and experiments to study helium discharges (99.999% purity) sustained by surface-wave discharges ($f = 2.45$ GHz), in capillary tubes ($R = 3$ mm radius) at atmospheric pressure ($p = 760$ Torr). Simulations use a self-consistent homogeneous and stationary collisional-radiative model (CRM) that solve the rate balance equations for the different species present in the plasma (electrons, He^+ and He_2^+ ions, He($n \leq 6$) excited states and He_2^* excimers) and the gas thermal balance equation, coupled to the two-term electron Boltzmann equation (including direct and stepwise inelastic and superelastic collisions as well as electron-electron collisions). Experiments use optical emission spectroscopy diagnostics to measure the electron density (H_β broadening), n_e, gas temperature (ro-vibrational transitions of OH, present at trace concentrations), T_g and the populations of different excited states. Model predictions at $n_e = 1.7 \times 10^{13}$ cm^{-3} are in agreement with measurements of (i) the excitation spectrum and excitation temperatures ($T_{exc} = 2795$ K, obtained from the Boltzmann-plot of the excited state populations), (ii) the power coupled to the plasma ($P_{abs} \sim 180 \pm 10$ W for a column length of $L \sim 1$ cm) and (iii) the gas temperature ($T_g \sim 1700 \pm 100$ K). Model results depend strongly on n_e, hence on plasma conductivity and the power coupled to the plasma. The coupling of a thermal module to the CRM has shown to be crucial. Increasing the electron density leads to very high gas temperature values, which limits the space of (n_e, T_g) as input parameters to the model.

1 Introduction

Over the last years, atmospheric-pressure plasmas have proven their potential for vast technological and industrial applications. Among these atmospheric-pressure plasmas, the surface-wave sustained discharges [1, 2, 3, 4, 5], have proven to be a very attractive tool for various applications (e.g. sample analysis [6], noble gas purification [7], surface treatments [8], laser sources [9], spectroscopy sources [10], ion sources [11], film deposition [12], etc). A great deal of the success of SWDs results from their extraordinary flexibility, operating over a large window of work conditions in pressure, power, wave frequency, dimensions and geometry. These discharges can be produced efficiently at frequencies ranging from a few hundreds of kHz to 10 GHz. The gas pressure that can be used ranges from the sub-millitorr domain up to a few times the atmospheric pressure. Discharge tube diameter include capillary tubes (0.5 mm) up to 10 cm.

As many other rare gases, helium is often used as a buffer gas in different plasma applications. For instance, in the field of analytical spectroscopy, helium atmospheric-pressure discharges are considered as most suitable for the detection of traces of nonmetal analytes with a high ionization potential (e.g. C, Cl, Br). In particular, helium SWDs sustained in capillary tubes and operated at microwave frequencies [6, 13, 14] have proved to be well adapted to a wide range of conditions. The possibility to modify the residence time of the samples (by varying either the gas flow or the plasma length through the power supplied to the discharge) without compromising the stability of the discharge makes the SWDs in helium very interesting tools for analytical purposes. The performance of these SWDs in analytical spectroscopy depends crucially on the kinetic mechanisms that leads to the excitation, ionization and dissociation of the analytes. Since the helium excited states are characterized by high energy excitation thresholds (≥ 19.82 eV), helium is more efficient to populate the excited state levels and ions of the samples to be analysed then other rare gases.

A deep knowledge of the fundamental processes governing these discharges and the physical quantities necessary for a complete understanding of the plasma medium is thus of great importance. For this reason the development of state-of-the-art collisional-radiative models (CRM) in pure helium at atmospheric pressure is needed, before moving to more complex scenarios for instance involving mixtures of helium with other gases.

CRMs are simulation tools of paramount importance for the kinetic description of discharge plasmas. The aim of these models is to obtain the populations of the different charged and excited species with the gas/plasma system as well as their effective creation/loss rates, relating them with the discharge maintence characteristics. Model solution requires knowledge about collisional-radiative data (cross sections for interaction with electrons, rate co-

efficients or frequencies for interactions between heavy species) and transport parameters for which one should couple the rate balance equations of the different species to the electron Boltzmann equation (EBE).
In particular, the inclusion of a thermal module in a CRM is a matter of great importance because there is a restrictive dependence of the gas temperature values with the electron density, (hence with the power coupled to the plasma). In order to determine this relationship, one must solve simultaneously the power balance equations for the neutrals and the electrons. In order to circunvent this complication, the great majority of published works in helium use both the electron density and the gas temperature as input parameters to the model, which can lead to unphysical results.
The typical validation of a CRM involves the comparison between predicted and measured values of the population densities with the main excited species of the plasma, obtained under the same work conditions. Usually, the densities of excited species are measured by OES diagnostics, which can also be used to obtain the electron density and the gas temperature.
The main objective of this work is the development and validation of a stationary and homogeneous self-consistent CRM for helium microwave capillary discharges (2.45 GHz), produced in cylindrical geometry (3 mm radius) at atmospheric pressure. The model is validated by OES measurements (to measure the electron density, the gas temperature and the population of the different excited states) performed on capillary surface-wave discharges at atmospheric pressure. The extreme dependence of model results (particulary the gas temperature and the power coupled to the plasma) on the electron density is also discussed.

2 Model formulation

The model solves the transport equations for the electrons and the ions, the particle balance equation for the excited state populations, the gas thermal balance equation to obtain the gas temperature, and the electron Boltzmann equation considering several direct and stepwise electron collisional processes.

2.1. Kinetic scheme

The model adopts an updated kinetic scheme that considers several electron-impact and heavy-species collisional mechanims involving the atomic excited states $\mathrm{He}(n,l,s) \equiv n^{2s+1}l$ (where n, l and s are the principal, the orbital and the spin quantum numbers, respectively), the excimers He_2^* and the atomic, He^+, and molecular, He_2^+, ions. The CRM developed in this work considers all the neutral states up to the level $n = 7$, so that the population densities for the first $n \leq 6$ excited states can be calculated with increased accuracy; the level $n = 7$ is then considered as a loss reservoir for the remaining states. The energy sublevels with $l =$ F,G,H,I of a given singlet ($s = 0$) or triplet ($s = 1$) energy level have been lumped into a single state with a single energy threshold. The electron kinetics is described by solving the corresponding Boltzmann equation (including 1st and 2nd order inelastic collisions, as well as electron-electron collisions), using a coherent set of electron cross sections appropriately adjusted to ensure good predictions of swarm parameters. The rate balance equations include electron-impact collisions (excitation / de-excitation / dissociation and ionization / recombination), atomic collisions (Penning reactions, l-exchange reactions, associative ionization, three-body association and dissociation), ion collisions (three-body ion conversion / dissociation), radiative transitions and transport. Table 1 summarizes the collisional and the radiative processes used in the model.

2.2. Model equations

In order to determine the non-equilibrium EEDF, $f(u)$, from wich all the electron rate coefficients and transport parameters (necessary to solve the model) can be calculated, the CRM developed in this work is coupled to the stationary and homogeneous EBE [22], written under the classical two-term expansion in spherical harmonics and assuming the DC effective field approximation. Inelastic and superelastic collisions of electrons with excited levels are considered only for the most populated states, 2^3S, 2^1S and 2^3P.

2.2.1.The electron mean power balance equation

The mean power balance equation per electron can be obtained multiplying the homogeneous EBE by the electron energy, u, and integrating it over all energies to obtain

$$\theta + P_{sup} = P_{el} + P_{exc} + P_{ion} \quad . \tag{1}$$

The two terms on the LHS of equation (1) represent, in order, the mean power absorbed from the HF field per electron, θ, and the mean power gained in superelastic collisions. The terms in the RHS represent, respectively, the mean power lost in elastic collisions with ground-state atoms, in excitations and in ionizations. The expressions for the different terms in equation (1) are very well known and they can be found in [22]. The power absorbed by the plasma, per unit lenght, dP_{abs}/dz (in Wcm^{-1}), can be estimated using the expression

$$\frac{dP_{abs}}{dz} = \theta n_e e \pi R^2 \tag{2}$$

$$= Re[\mu_{HF}] n_e e E^2 \pi R^2 \tag{3}$$

$$= Re[\sigma_{HF}] E^2 \pi R^2 \tag{4}$$

where e and n_e are, in order, the electron charge and density, R is the discharge radius, E is the RMS intensity of the applied HF electric field, and μ_{HF} and σ_{HF} are, respectively, the HF electron mobility and plasma conductivity.

Table 1: Summary of the collisional and the radiative processes and transport parameters adopted in this work. The label EEDF means that the rate coefficient was obtained by integration of the corresponding cross section over the electron energy distribution function; T_e and T_g are the electron and the gas temperature, respectively. The rate coefficients are in cm^3 s^{-1} unless specified otherwise.

Nb.	**Reaction**	**Rate coefficient**	**References**
	Electron-impact excitation, de-excitation and ionization	C_i^j	
(1)	$He + e \longrightarrow He + e$	EEDF	[15, 16]
(2)	$He(n,l,s) + e \longleftrightarrow He(n',l',s') + e$	EEDF	[16, 17]
(3)	$He(n,l,s) + e \longrightarrow He^+ + e + e$	EEDF	[15, 16, 17]
	Electron-impact recombination and dissociation	C_i^j	
(4)	$He_2^* + e \longrightarrow He_2^+ + e + e$	$9.75 \times 10^{-10} T_e(\mathrm{eV})^{0.71} \exp[\frac{-3.4}{T_e(\mathrm{eV})}]$	[18]
(5)	$He_2^+ + e \longrightarrow He(2^3S) + He$	$5.0 \times 10^{-9} [\frac{T_g}{T_e}]$	[19]
(6)	$He^+ + e + e \longrightarrow He(2^3S) + e$	$1.1 \times 10^{-14} [\frac{T_g^{2.3}(\mathrm{K})}{T_e^{4.5}(\mathrm{K})}]$ cm^6 s^{-1}	[16]
(7)	$He_2^+ + e + e \xrightarrow{b_r} He(2^3S) + He + e$	$1.1 \times 10^{-14} [\frac{T_g^{2.3}(\mathrm{K})}{T_e^{4.5}(\mathrm{K})}]$ cm^6 s^{-1}	[16]
	$\xrightarrow{1-b_r} He_2^* + e$		[16]
(8)	$He_2^* + e \longrightarrow 2He + e$	4.0×10^{-9}	[20, 21]
	Heavy particle collisions	$K_{k,i}^j$	
(9)	$He(n,l,s) + He \longrightarrow He_2^+ + e$		[16, 22]
(10)	$He(2) + He(2) \xrightarrow{b_p} He^+ + He + e$	$2.9 \times 10^{-9} [\frac{T_g(\mathrm{K})}{300}]^{-1.86}$	[16, 22]
	$\xrightarrow{1-b_p} He_2^+ + e$		[16, 22]
(11)	$He(n,l,s) + He \longrightarrow He(n,l',s) + He$	See text	[22]
(12a)	$He^+ + 2He \longrightarrow He_2^+ + He$	$1.4 \times 10^{-31} [\frac{T_g(\mathrm{K})}{300}]^{-0.6}$ cm^6 s^{-1}	[16, 22]
(12b)	$He_2^+ + He \longrightarrow He^+ + 2He$	$[\frac{1.4 \times 10^{-6}}{T_g^{-0.6}(\mathrm{K})}] \exp[\frac{-28100}{T_g(\mathrm{K})}]$	[16]
(13)	$He(2^3P) + 2He \longrightarrow He_2^* + He$	1.6×10^{-32} cm^6 s^{-1}	[16]
(14)	$He(2^3S) + 2He \longrightarrow He_2^* + He$	1.5×10^{-34} cm^6 s^{-1}	[16]
(15)	$He_2^* + He \longrightarrow He(2^3P) + 2He$	3.6×10^{-14}	[16]
	Radiative transitions	A_i^j	
(16)	$He(n,l,s) \xrightarrow{A_i^j \Lambda_{ji}} He(n', l \pm 1, s) + h\nu$	$4.333 \times 10^7 (\Delta u_i^j)^2 (\frac{g_j}{g_i}) f_{ji}$ s^{-1}	[22]
	Transport of heavy particles		
	Species		
(17a)	$He(2^3S)$	$D_M = 8.922 \times 10^{-2} [\frac{T_g(\mathrm{K})^{1.5}}{p(\mathrm{Torr})}]$ cm^2 s^{-1}	[22]
	$He(2^1S)$		[22]
(17b)	He_2^*	$D_* = 7.102 \times 10^{-2} [\frac{T_g(\mathrm{K})^{1.5}}{p(\mathrm{Torr})}]$ cm^2 s^{-1}	[19]
(18a)	He^+	$\mu_a N = A[B\sqrt{T_g(\mathrm{K})} + C]^{-1}$cm^{-1} V^{-1} s^{-1}	[16, 22]
		$A = 2.68 \times 10^{19}$	
		$B = 2.96 \times 10^{-3}$; $C = 3.11 \times 10^{-2}$	
		$D_a N = \mu_a N \frac{k_B T_g}{e}$	
(18b)	He_2^+	$\mu_m N = 2.6 \times 10^{19}$ cm^{-1} V^{-1} s^{-1}	[16]
		$D_m N = \mu_m N \frac{k_B T_g}{e}$	

2.2.2.The particle rate balance equations

At atmospheric pressure, the production of secondary electrons and the electrons loss by difusion and recombination are expected to have only second-order effects on the EEDF, so they are neglected in the homogeneous EBE [23]. Therefore, one must resort to the continuity equation to describe the electron balance. Accordingly, the model couples the EBE (representing the electron mean power balance equation) with a set of macroscopic particle rate balance equations for the charged particles (electron, atomic and molecular helium ions) and the helium excited states (atoms and excimers), taking into account the elementary processes given in table 1.
Under steady-state conditions, the rate balance equation for a given charged/excited species j has the form

$$\vec{\nabla}_r \cdot (n_j \vec{v}_{dj}) = S_j \tag{5}$$

where $n_j \vec{v}_{dj}$ is its flux and S_j its net production rate per unit volume. In the high-pressure regime considered here, the plasma is characterized by cross-section averaged quantities, considering an EEDF in local equilibrium with the radial average electric field, and the ambipolar diffusion approximation [16] to write equation (5) for the charged species as a 0D equation

$$\vec{\nabla}_r \cdot (n_j \vec{v}_{dj}) \approx \frac{D_{a,j}}{\Lambda^2} n_j = S_j \quad . \tag{6}$$

Here, $D_{a,j}$ is the ambipolar diffusion coefficient and $\Lambda \equiv R/2.405$ is the caracteristic diffusion length for a cylindrical vessel. The expressions of the ambipolar diffusion coefficients for electrons, atomic and molecular ions are given, respectively, by

$$D_{a,e} = \frac{n_a (\mu_a D_e + \mu_e D_a) + n_m (\mu_m D_e + \mu_e D_m)}{n_a \mu_a + n_m \mu_m + n_e \mu_e} \tag{7}$$

$$D_{a,a} = \frac{n_m (\mu_m D_a - \mu_a D_m) + n_e (\mu_a D_e + \mu_e D_a)}{n_a \mu_a + n_m \mu_m + n_e \mu_e} \tag{8}$$

$$D_{a,m} = \frac{n_a (\mu_a D_m - \mu_m D_a) + n_e (\mu_m D_e + \mu_e D_m)}{n_a \mu_a + n_m \mu_m + n_e \mu_e} \ , \tag{9}$$

where N_J, μ_j and D_j are, respectively, the density, mobility and the free diffusion coefficient of the given charged species j (for the atomic and molecular ions see (18a) and (18b) in table 1); for the electrons μ_e and D_e are obtained as energy integrals over the EEDF. The model assumes that the loss rate to the wall of electrons and atomic and molecular ions is nearly the same, so the previous coefficients must satisfy

$$n_a D_{a,a} + n_m D_{a,m} \approx n_e D_{a,e} \quad . \tag{10}$$

Using the creation/loss elementary processes presented in table 1 the homogeneous and steady-state continuity equation for a given species j writes

$$\sum_{i \neq j} n_e n_i C_i^j + \sum_{i>j} n_i A_i^j \Lambda_{ji} + \sum_{k,i} n_k n_i K_{k,i}^j = \sum_{i \neq j} n_e n_j C_j^i + \sum_{i<j} n_j A_j^i \Lambda_{ij} + \sum_{k,i} n_i n_j K_{i,j}^k + \frac{D_j}{\Lambda^2} n_j + \frac{n_j}{\tau} \tag{11}$$

Here C_i^j represents the $i \to j$ excitation/de-excitation electron rate coefficient, $A_i^j \Lambda_{ji}$ the Einstein transition probability for the $i \to j$ transition multiplied by the corresponding escape factor, $K_{k,i}^j$ the rate coefficient for $k, i \to j$ atomic collisions, $\tau = V_d/Q$ is a residence time (with V_d the discharge volume and Q the gas flow and D_j the diffusion coefficient of species j. Therefore, the terms on the LHS of equation (11) represent, respectively, the net production rate of species j due to electron-impact collisions with species i, radiative transitions from the excited states i and atomic collisions between the species k and i. The terms on the RHS represent, in order, the net loss rate of species j due to its collisions with electrons, radiative transitions to the excited states i, atomic collisions with the species i, diffusion and flow.
Transport phenomena (diffusion and flow) were taken into account for the charged particles, the metastable states and the excimers. Therefore, in equation (11) one has $D_j = D_{a,j}$ if applied to a charged particle, $D_j = D_M$ if applied to the metastable (2^3S and 2^1S) states, and $D_j = D_*$ if applied to the excimers, where D_M and D_* are the diffusion coefficients for the metastables and the excimers, respectively (see (17a) and (17b) in table 1).
Since the ionization degrees, n_e/N, are smaller than 10^{-5} and $\sum_j n_j \ll N$, the gas density, N, can be calculated from the ideal gas equation and therefore the rate balance equation for the ground-state 1^1S is not solved. One should also note that the ionization-loss rate balance equation for the atomic ions can be linearly obtained, under ambipolar conservative conditions, from the corresponding rate balance equations for the electrons and the molecular ions (see equation (10)).

2.2.3.The gas thermal balance equation

The average gas temperature, $< T_g >$, can be calculated by solving the stationary gas thermal balance equation which, in the absence of gas flow, writes

$$\vec{\nabla} \cdot \left(-\lambda \vec{\nabla} T_g + \sum_j m_j C_{p_j} T_g \vec{\Gamma}_j \right) = \sum_j e \vec{\Gamma_j} \cdot \vec{E}_s + n_e \theta_{el} \quad , \tag{12}$$

where $\lambda = 1.52 \times 10^{-1} \, (T_g/300)^{0.71}$ W m^{-1} K^{-1} [24] is the thermal conductivity of helium; $m_j C_{p_j} \simeq (5/2) k_B = 3.45 \times 10^{-23}$ J K^{-1}, $\vec{\Gamma}_j = -D_{a,j} \vec{\nabla} n_j$ and $\vec{E}_s = -u_k \vec{\nabla} n_e / n_e$ are, respectively, the heat capacity, the ion particle flux and the space-charge electric field [25]; $u_k \equiv D_e N / \mu_e N$ is the characteristic energy for electrons and θ_{el} is the mean power lost per electron due to elastic collisions with neutral gas particles.
In equation (12), the first and second terms in LHS represent, in order, the power transfer due to conduction and convection (i.e. the transport of thermal energy due to the transport of particles), whereas the terms in the RHS represent, respectively, the power gained by the gas due to the flux of ions under the influence of

the space-charge electric field and due to elastic collisions with electrons. Note that we have not considered the power transfer channels between electrons and the gas due to inelastic and superelastic collisions, which are negligible in the atmospheric pressure region (see section 4).

In a homogeneous 0D description, the gas thermal balance equation (12) is averaged over the discharge volume $V_d = 2\pi R^2 L$ (with L the discharge length) which, assuming axial homogeneity gives

$$\begin{aligned}\left[-\lambda \left.\frac{dT_g}{dr}\right|_R - \sum_j m_j C_{p_j} D_{a,j} \left.\frac{dn_j}{dr}\right|_R T_g(R)\right] 2\pi RL \\ = \quad 2\pi L \sum_j e D_{a,j} u_k \int_0^R \frac{dn_j}{dr}\frac{d\ln n_j}{dr} r dr + \\ + \quad \theta_{el} 2\pi L \int_0^R n_e r dr \,, \end{aligned} \tag{13}$$

where we have used the hypothesis of congruence $\nabla_r n_j/n_j \simeq \nabla_r n_e/n_e$. Assuming a parabolic profile for the gas temperature and a Bessel profile for the charged-particle densities (obtained, respectively, from the solution to $\vec{\nabla}\cdot\left(-\lambda\vec{\nabla}T_g\right) = C$ and $\vec{\nabla}\cdot\left(-D_j\vec{\nabla}n_j\right) = n_j\nu_j$ in cilindrical coordinates, with C a constant and ν_j the ionization frequency of ion species j if also assumed constant) one gets

$$T_g(r) = T_{g_0}\left(1 - \frac{r^2}{R^2}\right) + T_{g_W}\frac{r^2}{R^2} \tag{14}$$

$$n_j(r) = n_{j_0} J_0(r/\Lambda) \quad , \tag{15}$$

where T_{g_0} and T_{g_W} are, respectively, the gas temperature at $r = 0$ (discharge axis) and $r = R$ (discharge wall); n_{j_0} is the charged particle density of ion species j at $r = 0$; and J_0 is the 0th-order Bessel function, J_n, of the first kind. Because the radial average of a given quantity $X(r)$ is given by

$$\langle X(r)\rangle = \frac{2\int_0^R X(r) r dr}{R^2} \quad , \tag{16}$$

one can easily chek that

$$\left.\frac{dT_g}{dr}\right|_R = \frac{4}{R}\left(T_{g_W} - \langle T_g\rangle\right) \tag{17}$$

$$\left.\frac{dn_j}{dr}\right|_R = -\frac{x_W^2}{2R}\langle n_j\rangle \quad , \tag{18}$$

with $x_W = 2.405$. Using equations (17) and (18) in equation (13) one obtains

$$\begin{aligned} 8\lambda\left(\langle T_g\rangle - T_{g_W}\right) + x_W^2 T_{g_W}\sum_j m_j C_{p_j} D_{a,j}\langle n_j\rangle \\ = \quad \int_0^{x_W} \frac{J_1^2(x)}{J_0(x)} x dx \sum_j e D_{a,j} u_k \frac{x_W}{J_1(x_W)}\langle n_j\rangle \\ + \quad R^2\theta_{el}\langle n_e\rangle \,, \end{aligned} \tag{19}$$

where $x \equiv r/\Lambda$. In principle, equation (19) provides a straighfoward solution to $< T_g >$. However, the integral

$$\beta \equiv \int_0^{x_W} \left(J_1^2(x)/J_0(x)\right) x dx \quad , \tag{20}$$

diverges when calculated numerically, since $J_0(x_W) = 0$. To solve this problem, one needs to estimate $[J_1/J_0](x_W)$ by writing the integral β in a discrete form and using the actual value of the space-charge potential at the wall. Taking into account that

$$\begin{aligned} E_s &= -u_k \frac{J_1(x)}{J_0(x)}\frac{1}{\Lambda} \\ &= -\frac{dV}{dr} \quad , \end{aligned} \tag{21}$$

where V is the space-charge potencial drop, and dividing R into l equally spaced cells of length Δr (so that $x_i = i\Delta x$, $\Delta x = \Delta r/\Lambda$ and $x_l = l\Delta x \equiv x_W$), one can check, after some algebra, that

$$\frac{J_1(x_W)}{J_0(x_W)}\Delta x = \frac{V(x_W)}{u_k} - \sum_{i=0}^{l-1}\frac{J_1(x_i)}{J_0(x_i)}\Delta x \quad . \tag{22}$$

Therefore, the integral β in equation (19) can be written in its discrete form as

$$\begin{aligned} \beta &\equiv \sum_{i=0}^{l}\frac{J_1^2(x_i)}{J_0(x_i)} x_i \Delta x \\ &= \sum_{i=0}^{l-1}\frac{J_1^2(x_i)}{J_0(x_i)} x_i \Delta x + \\ &+ J_1(x_W) x_W \left[\frac{V(x_W)}{u_k} - \sum_{k=0}^{l-1}\frac{J_1(x_k)}{J_0(x_k)}\Delta x\right] . \end{aligned} \tag{23}$$

Equation (19) can be solved to yield a finite β-value, if the wall potential is replaced by its actual value [26]

$$V_j(R) = -\frac{k_B T_e}{2e}\ln\left(\frac{\pi m_e}{2M}\right) \simeq 4.22 u_k \quad . \tag{24}$$

By using (23) - (24) into (19) it is possible to solve the latter for $< T_g >$, given R, $< n_e >$ and the boundary conditions T_{g_W}, the obtained densities $< n_j >$ and the characteristic energy u_k from the CRM, and knowing the values of the different transport parameters and power-transfer quantities. Notice that the dependence of λ on $< T_g >$ requires adopting an iterative scheme in solving (19). In the following, and for the sake of simplicity, the radially averaged quantities $< T_g >$, $< n_j >$, $< n_e >$ will be denoted simply as T_g, n_j, n_e, dropping the symbol $< \cdot >$ whenever this causes no confusion.

3 Experimental setup and work conditions

Experiments are based on the following OES diagnostics: the Stark broadening of the H_β line transition, which is used to obtain the electron density, n_e; (ii) the rotational

spectrum of the OH radical (present at trace concentrations), which is fitted to deduce the rotational temperature, T_{rot} (assumed to represent the gas temperature T_g); (iii) the intensities of different spectral lines, related to the populations of the emitter (excited) states, whose Boltzmann-plot allows deducing the plasma excitation temperature, T_{exc}.

The helium (99.999 % purity) plasma column with $L \sim 1$ cm length is sustained inside a quartz tube with $R = 3$ mm radius at atmospheric pressure ($p = 760$ Torr) using a constant gas flow $Q = 2.1$ slm (standard liter per minute). The microwave power was supplied by a generator ($\omega/2\pi = 2.45$ GHz excitation frequency) and delivered with the help of a surfatron, as shown in figure 1.

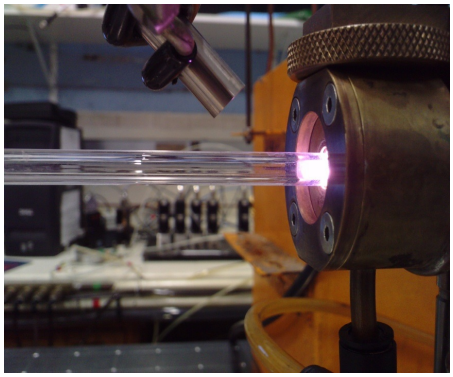

Figure 1: Image of the surface-wave discharge in helium at atmospheric pressure. Courtesy of Belmonte and Nöel (IJL).

4 Model validation and results

The model was solved for different values of electron densities, $n_e = (1.0 - 7.4) \times 10^{13}$ cm^{-3}, and for the experimental operation conditions discussed in section 3, i.e., taking as input parameters $p = 760$ Torr, $R = 3$ mm, $L = 10$ mm, $\omega/2\pi = 2.45$ GHz, $T_{g_W} = 600$ K and $Q = 2.1$ slm. The solution of the system formed by the ionization-loss balance equations for the charged particles and the rate balance equations for the excited states and excimers (see equation (11)), coupled with the homogeneous and stationary electron Boltzmann equation and the gas thermal balance equation (19) allow us to determine in a self consistent manner the value of the reduced electric field, E/N as an eigen value to the problem together with the EEDF (and all the electron transport parameters), the gas temperature, the population densities of the $n < 7$ excited states, the atomic and molecular ions and excimers as well their creation/loss rate.

4.1. Model validation

The solution of the model in the range of electronic densities considered here, reveals that the best agreement between calculations and experiments stands for $n_e = 1.7 \times 10^{13}$ cm^{-3}. For this value of electronic density, the solution of equation (19) returns a value for the gas temperature of $T_g = 1727$ K which is in very good agreement with the measured gas temperature ($T_g \sim 1700$ K) and the experimental electronic density of $(2.45 \pm 1.4) \times 10^{13}$ cm^{-3} (being the last obtained using the calculated value of electronic temperature, $T_e = 1.70$ eV). For this conditions, the calculated power absorbed by the plasma, per unit length, (see equation (4)) is $dP_{abs}/dz = 150$ W cm^{-1}, which is also in very good agreement with the experimental value of $P_{abs} = 180 \pm 10$ W for the plasma collum of $L = 1$ cm. In figure 2(a) is presented the calculated excitation spectrum, $\mathrm{Ln}(n_j g_0/N g_j)$ against the excitation energy u_j for $n_e = 1.7 \times 10^{13}$ cm^{-3} . In this figure the solid lines represents the best fits to Boltzmann distributions. One can see that the calculated spectrum does not follow a Boltzmann distribution and, at least, three excitation temperatures are needed to describe the distribution of the different excited states populations. Results suggest that ground state and excited states with excitation energies lying between 0 eV and 21.218 eV (i.e. from 2^3S up to 2^3P states) follows a Boltzmann distribution characterized by an excitation temperature $T_{exc} \approx 1$ eV, closer to the electron temperature ($T_e = 1.7$ eV). The excited states populations with excitation energies lying between 22.718 eV and 24.209 eV (from 3^3S up to 6^1D), approximately follow a Boltzmann distribution at an excitation temperature $T_{exc} = 2717$ K. The last fit was performed for energies lying between 23.972 eV and 24.211 eV (from 5^3S up to 6^1P) with a resulting excitation temperature, $T_{exc} = 1577$ K, closer to the gas temperature ($T_g = 1727$ K).

The comparison between the calculated and measured excitation spectrum is shown in figure 2(b). For comparison, it was only taken into account the calculated values of the excited states populations that were common to those measured by optical emission spectroscopy in the energy region between 22.718 eV and 23.972 eV. It was found that the model prediction of the excitation temperature, $T_{exc} = 2785$ K, were in excellent agreement with the experimental value, $T_{exc} = 2793$ K.

4.2. Model results as a function of the electron density

Table (2) shows the values of the different average fractional powers channels tranfered by collisions between electrons and the atoms as well the values of θ/N, dP_{abs}/dz, T_e and N for various n_e. Results show that the power absorbed from the field, by electrons, is mostly lost by elastic collisions with the ground state atoms. The power gain/loss due to superelastic and inelastic collisions is shown to be negligible. Results support the choice in negleting the power transfer channels do to inelastic and superelastic collisions when solving the gas thermal balance equation in the region of atmospheric pressure. However, one should note that this assumption may note

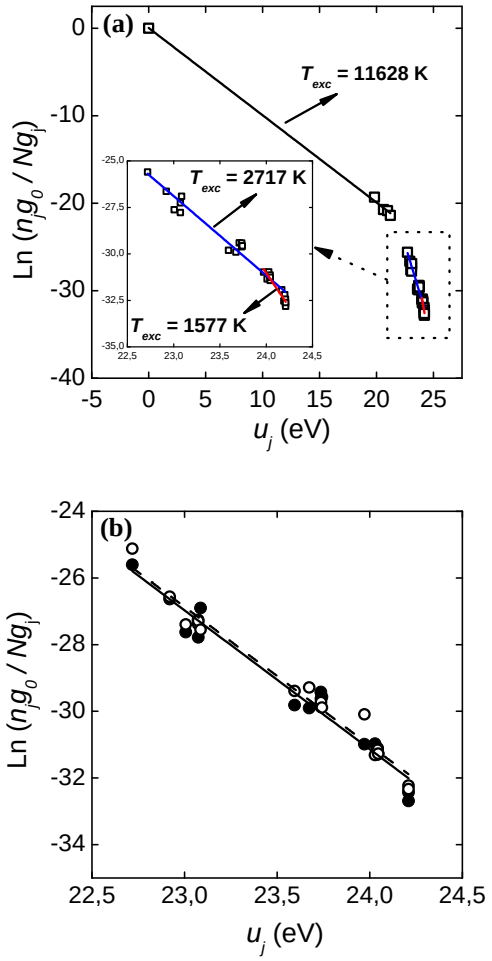

Figure 2: (a) Excitation spectrum calculated for $n_e = 1.7 \times 10^{13}$ cm^{-3}. The solid lines results from the best fits to Boltzmann distribution for $u_j = 0 - 21.218$ eV ($T_{exc} = 11628$ K), $u_j = 22.718 - 24.209$ eV ($T_{exc} = 2717$ K) and $u_j = 23.972 - 24.211$ eV ($T_{exc} = 1577$ K). (b) Comparison of the calculated (•) and experimental (○) excitation spectrum common to both model and experiment. The calculated spectrum was performed for the same value of electron density as in (a) and for the experimental operation conditions. The lines results from the best fits to Boltzmann distribution for $u_j = 22.718 - 24.209$: full line, model ($T_{exc} = 2785$ K); broken line, experiment ($T_{exc} = 2793$ K).

be valid for low pressure regimes, where inelastic collisions take an important role in the power transfer as it is shown in [22]. The power absorbed by the plasma per unit lenght is found to increase with increasing electron density, which is a consequence of a higher plasma conductivity (see equation (4).

Figure (3) shows the calculated values of the effective field, E_{eff}/N and the gas temperature as a function of the electron density. The points indicates the values of these quantities for the same experimental conditions with $n_e = 1.7 \times 10^{13}$ cm^{-3} but with $T_{gw} = 300$ K. As n_e increases results show a decreasing on the E_{eff}/N values. An increasing electron density leads to a higher efficiency in ionization, hence the electric field needed to maintain the discharge is lower.

Model results show that the gas temperature depends strongly on n_e, hence on plasma conductivity and the power coupled to the plasma. This result reinforces the previous statement regarding the importance of coupling a thermal model to the CRM. Increasing electron density leads to very-high values of the gas temperature values, limiting the space of n_e and T_g as input parameters to the model. In fact, this restrict relationship between T_g and n_e can be better understood when looking to the different power transfer channels in equation (19). The solution of the thermal model reveals that the gas power gain and losses are due to electron-neutral elastic collisions and conduction, respectively, while the flux and convection terms are negligible in the power balance. Results also show that decreasing the gas temperature on the discharge wall T_{g_W} from 600 K to 300 K, is reflected by a decrease of T_g from 1727 K to 1597 K.

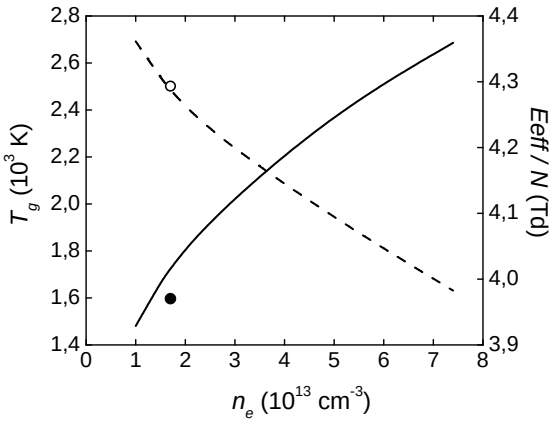

Figure 3: Calculated gas temperature (full curve) and effective field (broken curve) as a function of the electron density, for $p = 760$ Torr, $R = 3$ mm, $Q = 2.1$ slm and $T_{gw} = 600$ K (experimental operation conditions). The dots indicates the values of T_g (•) and E_{eff}/N (○) with $T_g^{wall} = 300$ K for $n_e = 1.7 \times 10^{13}$ cm^{-3}.

Figure 4(a) shows the calculated reduced population densities of helium atomic and molecular ions as a function n_e and for the experimental operating conditions. One can see that, throughout most of the considered electronic density range, the He_2^+ is the predominant ion. For $n_e = 1.7 \times 10^{13}$ cm^{-3} the density ratio $[He_2^+]/[He^+]$ is ≈ 200. However, as n_e increases, this ratio becomes smaller and for $n_e \geq 6 \times 10^{13}$ cm^{-3} the ratio $[He_2^+]/[He^+]$ starts decreasing from 1 to 0.5. These results show that the atomic ions becomes the dominant ion as n_e increases, hence with increasing gas temperature.

The calculated reduced populations densities of the metastables states 2^3S and 2^1S, radiative states 2^3P and 2^1P and the helium excimers He_2^* are plotted, as a function of n_e, in figure 4(b). One can see that the density of

Table 2: Model results for the different fractional power transfer channels for electron-atom collisions, the average power absorbed per electron divided by the gas density, the power aborbed by the plasma per unit lenght and the electron temperature, as a function of n_e and for the experimental operating conditions.

n_e (cm^{-3})	N (cm^{-3})	θ_{ela} (%)	θ_{ine} (%)	θ/N (eV cm^3 s^{-1})	dP_{abs}/dz (W cm^{-1})	T_e (eV)
1.0×10^{13}	$4,96 \times 10^{18}$	99.95	0.05	4.67×10^{-11}	105	1.72
1.5×10^{13}	$4,41 \times 10^{18}$	99.94	0.06	4.59×10^{-11}	137	1.71
1.7×10^{13}	$4,25 \times 10^{18}$	99.93	0.07	4.57×10^{-11}	150	1.70
2.5×10^{13}	$3,79 \times 10^{18}$	99.90	0.10	4.49×10^{-11}	193	1.69
5.0×10^{13}	$3,07 \times 10^{18}$	99.80	0.20	4.32×10^{-11}	300	1.67
7.4×10^{13}	$2,73 \times 10^{18}$	99.77	0.23	4.14×10^{-11}	379	1.64

the helium excimers population is not neglegible when compared to the most populated excited states populations. In fact, for $n_e = 1.7 \times 10^{13}$ cm^{-3}, the density ratio $[He(2^3S)]/[He_2^*]$ it is found to be ≈ 1.2. These results justify the inclusion in the model the kinetics of helium excimers in the region of atmospheric pressure.
Figure 5 shows the fractional production and destruction rates of electrons as a function of n_e and for experimental operation conditions. One can see that electrons are mainly created by associative ionization and destroyed by dissociative recombination with the molecular ions.
In figure 6 the fractional production and destruction rates of helium atomic ions are plotted against n_e. One can observe that atomic ions are mainly destroyed and created by the 3-body ionic conversion and its reverse reaction, respectively. Direct ionization by electron impact becomes, however, an important mechanism in creating He^+ ions for low electronic densities.
The fractional production and destruction rates of helium molecular ions are showned in figure 7. Associative ionization and dissociative recombination play, respectively, an important role in the production and destruction of He_2^+ in the region of low electronic densities. Similary to the atomic ions, and for $n_e \geq 3 \times 10^{13}$ cm^{-3}, molecular ions are mainly created and destroyed by the 3-body ionic conversion and its reverse reaction. These results, together with the ones shown in figure 4(a), indicates that the mechanism of ionic conversion becomes more efficient in creating atomic ions with increasing electronic density, hence with increasing gas temperature.
Although we decided no to depicte the production/destruction rates for 2^3S metastable state, model results shows that this state is mainly produced by superelastic electron collisions and radiative transitions involving all the excited states above it (which show that metastable states can be regarded as an energy reservoir), and destroyed only by stepwise inelastic collisions with electrons (indicating that stepwise inelastic processes from metastables are important in the plasma kinetics).
The 2^3P state is mainly created, throughout most of the considered range of electronic densities, by inelastic electron collisions with the metastables and mainly destroyed by radiative trasitions (for low n_e values) and by collisions with neutral in the mechanism of excimers production (for higher n_e). These results show that the

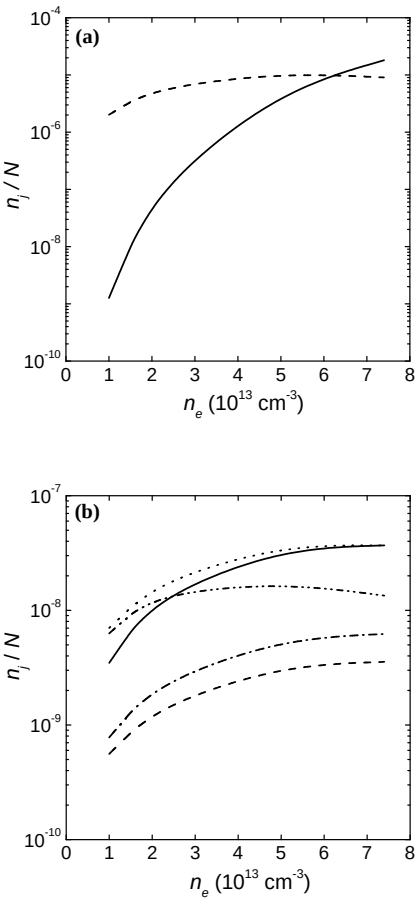

Figure 4: (a) Atomic (full curve) and molecular ions (broken curve) densities divided by the gas density as a function of the electron density. (b) 2^3S (dotted curve), 2^1S (dashed curve), 2^3P (full curve), 2^1P (dashed dotted curve) and excimers (dashed dotted dotted curve) population densities divided by the gas density as a function of the electron density.

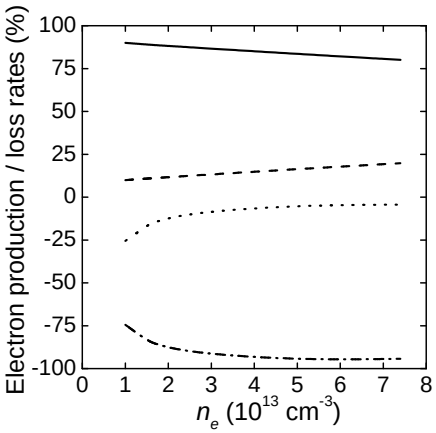

Figure 5: Fractional production/destruction rates for electrons as a function of the electronic density. The different curves correspond to the following production/destruction mechanisms (see table 1): dashed curve, reaction (3); full curve, reaction (9); dashed-dotted curve reaction (5) and dotted curve, diffusion.

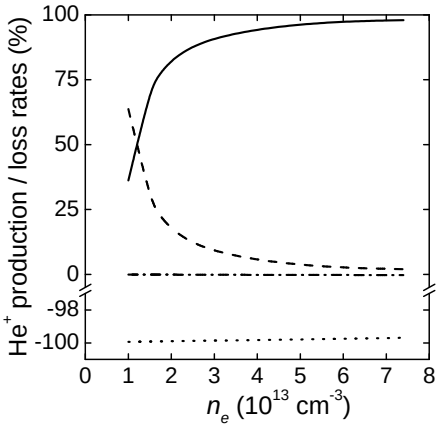

Figure 6: Fractional production/destruction rates for atomic ions as a function of the electronic density. The different curves correspond to the following production/destruction mechanisms (see table 1): full curve, reaction (12b); dashed curve, reaction (3); dotted curve, reaction (12a) and dashed-dotted curve, reaction (18a).

kinetics of the 2^3P state play an important role, besides the role played by a particular radiative state, in the kinetics of the He_2^* state. In fact, the He_2^* state is mainly created from the 2^3P state and destroyed by the reverse reaction (for low n_e values) and by dissociation (for high n_e values).

5 Conclusions

In this thesis surface-wave capillary plasma discharges produced in pure helium, at atmospheric pressure, were studied using both simulations and experiments. Experiments were based in optical emission spectroscopy diagnostics to obtained the electron density, the gas temperature and the population of different excited states. Simulations used a stationary and homogeneous collisional-radiative model (CRM) coupled with the electron Boltzmann equation and the gas power balance equation in order to calculate, in a self-consistent manner, E_{eff}/N, T_g, P_{abs} and the population densities of the atomic ions, the molecular ions and the $n < 7$ excited states of helium, as well as their creation/destruction rates, as a function of n_e and for the discharge parameters $p = 760$ Torr, $(\omega/2\pi) = 2.45$ GHz, $L = 1$ cm, $R = 0.3$ cm and $Q = 2.1$ slm.

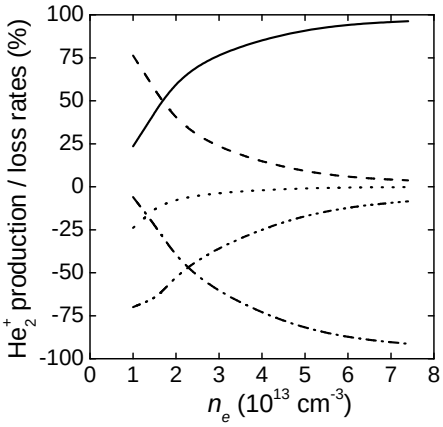

Figure 7: Fractional production/destruction rates for molecular ions as a function of the electronic density. The different curves correspond to the following production/destruction mechanisms (see table 1): full curve, reaction (12a); dashed curve, reaction (9); dashed-dotted curve, reaction (12b), dashed-dotted-dotted curve, reaction (5), reaction (18a) and dotted curve, reaction (18b).

All elementary processes included in the model were extensively discussed and an up-to-date information has been presented. In particular: (i) the set of electron scattering cross sections with helium (ground-sate and excited) atoms was upgraded and extended to energies up to 1 keV, with respect to a previous data set [15, 16]; (ii) the kinetic mechanisms with the CRM were revised and extended to atmospheric-pressure conditions, to include molecular species (He_2^* and He_2^+) and to consider gas temperature dependences (whenever possible) for the main rate coefficients and transport parameters with the heavy-species.

Model calculations (for $n_e = 1.7 \times 10^{13}$ cm^{-3}) were validated by comparison with experiments and a very good agreement was found (within the experimental uncertainties) for the gas temperature, the power coupled to the plasma, the excitation temperature and the excited states densities. A further validation can be envisaged, focusing on the variation of results with changes in the tube radius.

It was found that for the experimental conditions (i.e. for $n_e = 1.7 \times 10^{13}$ cm^{-3}): (i) He_2^+ is the predominant

ion and it is mainly created and destroyed, similarly to the electrons, by associative ionization and dissociative recombination, respectively; (ii) the He_2^* density is comparable with that of the most populated excited states, the radiative 2^3P state playing an important role in its production/destruction; (iii) Penning reactions and electron assisted recombination mechanisms do not play a significant role in the creation/loss of He(2) states and helium ions.

Model results exhibit a strong dependence on n_e, hence on the plasma conductivity and the power coupled to the plasma. The coupling of a thermal model to the CRM: (i) revealed that the gas power gain and loss mechanisms are due to electron-neutral elastic collisions and conduction, respectively; (ii) was crucial to ensure self-consistent meaningful results. Indeed, increasing the electron density leads to very-high gas temperatures, which limits the region of electron density values as input parameter. Hence, CRMs should include also gas power balance equation (especially at atmospheric pressure), instead of imposing both n_e and T_g as free parameters, a strategy adopted in many works. With this respect, dedicated measurements addressing the gas temperature dependence of rate coefficients and/or transport parameters are required to improve the quality of model results. The self-consistent model and the corresponding validated simulation tool developed in this work should be regarded as part of a wider research program, on the study of microwave-driven atmospheric-pressure microplasmas. In this context, the characterization of electrical discharges in gas mixtures containing helium (usually as dominant buffer element), with strong potential for applications, can directly benefit from the tool and results obtained here, to be used as starting point in future studies.model.

References

[1] M. Moisan; C. Beaudry and P. Leprince. *IEEE Trans. Plasma Sci.*, PS-3:55, 1975.

[2] Zakrzewski; M. Moisan; V. M. M. Glaude; C. Beaudry and P. Leprince. *Plasma Phys.*, 19:77, 1977.

[3] V. M. M. Glaude; M. Moisan; R. Pantel; P. Leprince and J. Marec. *J. Appl. Phys.*, 51:5693, 1980.

[4] M Moisan and Z Zakrzewsk. *J. Phys. D: Appl. Phys.*, 24:1025–1048, 1991.

[5] C. Boisse-Laporte; A. Granier; E. Bloyet; P. Leprince and J Marec. *J. Appl. Phys.*, 61(5):1740, 1987.

[6] K. C. Tran; C. Lauzon; R. Sing and J. Hubert. *J. Anal. At. Spectrom.*, 13:507, 1998.

[7] Kabouzi and M. Moisan. *IEEE Trans. Plasma Sci.*, 33:292, 2005.

[8] Moisan M; Barbeau J; Crevier MC; Pelletier J; Phillip N; Saoudi B. Plasma sterilization. *Methods Mech Pure Appl Chem*, 73:349–58, 2002.

[9] L Bertrand; M. Gagné R; G. Bosisio and M. Moisan. *IEEE Quantum Electron.*, QE-14:8, 1978.

[10] M Moisan; R. Pantel; J. Hubert; E. Bloyet; P. Leprince; J. Marec and A. Ricard. *J. Microwave Power*, 14:57, 1979.

[11] M. Moisan; C. M. Ferreira; Y. Hajlaoui; D. Henry; J. Hubert; R. Pantel; A. Ricard and Z. Zakrzewski. *Rev. Phys. Appl. (Paris)*, 17:707, 1982.

[12] S. Schelz; C. Campillo; M. Moisan. *Diamond and Related Materials*, 7:1675–1683, 1998.

[13] Stanley P. Wasik and Frederick P. Schwarz. *J Chromatogr Sci*, 18(12):660, 1980.

[14] Kiyoshi Tanabe; Hiroki Haraguchi; Keiichiro Fuwa. *Spectrochimica Acta Part B: Atomic Spectroscopy*, 36:633, 1981.

[15] Alves L L and Ferreira C M. *J. Phys. D: Appl. Phys.*, 24:581, 1990.

[16] Belmonte T; Cardoso R P; Henrion G and Kosior F. *J. Phys. D: Appl. Phys.*, 40:7343, 2007.

[17] Ralchenko Yu; Janev R K; Kato T; Fursa D V; Bray I; de Heer F J. *Atomic Data and Nuclear Data Tables*, 94:603, 2008.

[18] Yuan X and Raja L L. *IEEE Trans. Plasma Sci.*, 313:495, 2003.

[19] R. Deloche; P. Monchicourt; M. Cheret and F. Lambert. *Phys. Rev.*, A(13):1140, 1976.

[20] Emmert F; Angermann H H; Dux R and Langhoff H. *J. Phys. D: Appl. Phys.*, 21:667, 1988.

[21] Hill P C and Herman P R. *Phys. Rev.*, A 47:4837, 1993.

[22] Alves L L; Gousset G and Ferreira C M. *J. Phys. D: Appl. Phys.*, 25:1713, 1992.

[23] I Peres; L L Alves; J Margot; T Sadi; C M Ferreira; K C Tran and J Hubert. *Plasma Chemestry and Plasma Processing*, 19(4):467–486, 1999.

[24] Vargaftik N B and Vasilevskaya Yu D. *Inzhenerno-Fizicheskii Zhurnal*, 42:412, 1982.

[25] Luís L Alves. *Plasma Sources Sci. Technol.*, 16:557–569, 2007.

[26] Lieberman M A and Lichtenberg A J. Principles of plasma discharges and materials processing. 1994.